Delay in Photoemission

M. Schultze,[1,2]* M. Fieß,[2] N. Karpowicz,[2] J. Gagnon,[1,2] M. Korbman,[2] M. Hofstetter,[1] S. Neppl,[3] A. L. Cavalieri,[2] Y. Komninos,[4] Th. Mercouris,[4] C. A. Nicolaides,[4] R. Pazourek,[5] S. Nagele,[5] J. Feist,[5,6] J. Burgdörfer,[5] A. M. Azzeer,[7] R. Ernstorfer,[3] R. Kienberger,[2,3] U. Kleineberg,[2] E. Goulielmakis,[2] F. Krausz,[1,2] V. S. Yakovlev[1,2]*

Photoemission from atoms is assumed to occur instantly in response to incident radiation and provides the basis for setting the zero of time in clocking atomic-scale electron motion. We used attosecond metrology to reveal a delay of 21 ± 5 attoseconds in the emission of electrons liberated from the 2p orbitals of neon atoms with respect to those released from the 2s orbital by the same 100–electron volt light pulse. Small differences in the timing of photoemission from different quantum states provide a probe for modeling many-electron dynamics. Theoretical models refined with the help of attosecond timing metrology may provide insight into electron correlations and allow the setting of the zero of time in atomic-scale chronoscopy with a precision of a few attoseconds.

The emission of an electron from an atom upon the absorption of an energetic photon (photoemission, or the photoelectric effect) is one of the most elementary quantum-mechanical phenomena (1–3). In the absence of resonances, the formation of the outgoing wave packet is usually presumed to instantly follow temporal variations of the incident light field. A delayed response, the possibility of which was recognized in the 1950s (4, 5), would have several far-reaching consequences. If a single electron is set free when an atom absorbs a photon, it is, strictly speaking, not a single-electron process. Rather, it is the result of the correlated motion of all the electrons; hence, electron correlations generally affect the properties of the emitted photoelectron (6, 7). As a consequence, comprehensive attosecond-scale temporal characterization of photoemission promises new insights into intra-atomic electron correlations and can bolster theoretical models of dynamic changes of atomic structure (8) and of correlated many-electron dynamics.

Furthermore, a delay in photoemission implies a change in the timing of ejection of the electron pulse with respect to the arrival of the photon pulse. This would compromise the accuracy of setting the zero of time for clocking microscopic processes on the atomic time scale. Capturing the outgoing electron with the controlled

electric field of a laser pulse (9) via attosecond streaking (10, 11) provides the only means of timing the arrival of a photon pulse with a precision comparable to the atomic unit of time. This timing is of fundamental importance because attosecond light pulses (12–15) presently constitute the most precise trigger for timing electronic processes. Hence the zero of time in atomic-scale chronoscopy, the time-resolved observation of electronic and concomitant processes, is to coincide with the arrival time of this photon pulse. Any unknown delay Δt in the emission of the photoelectron wave packet will result in an apparent shift of the origin of the time arrow (Fig. 1A). This introduces an unknown systematic error in clocking the microscopic motion under scrutiny, preventing us from revealing its details. Reliable absolute timing information would be essential, for example, in understanding the multielectron response of metals and semiconductors to sudden excitations (16).

Our measurements reveal a small delay time between the formation of electron wave packets originating from different atomic orbitals. The temporal properties of both wave packets were recorded by means of attosecond streaking (10), and the measured spectrograms were found to be shifted with respect to each other along the pump-probe delay axis (henceforth referred to as temporally shifted), as if one of the wave packets were emitted later than the other. Comprehensive quantum simulations show that a delay of one wave packet with respect to the other indeed results in a temporal shift between spectrograms, even though the delay between wave packets and the shift between spectrograms may not be exactly equal to each other. The delay considered here is of a different physical origin than that previously observed in photoemission from a solid (17), where a temporal shift was attributed to transport effects that occur before an electron reaches the surface (18, 19).

Attosecond streaking measurements on Ne. Ne was chosen for our study for two reasons.

First, its small polarizability precludes the possibility of an artificial temporal shift of the spectrogram due to the Stark effect (20). Second, the relatively high photoionization cross-section (21) benefits the signal-to-noise ratio (S/N) of attosecond streaking, which is of crucial importance for achieving the required timing accuracy.

Even the most advanced measurements in photoelectron spectroscopy can only provide energy and angle-resolved probability distributions (22, 23). Probing the photoionization cross-section corresponds to measuring the absolute values of complex-valued matrix elements that quantum mechanics assigns to transitions from a bound atomic state to states where a photoelectron propagates toward the detector. The quantum phase of the matrix element, the energy derivative of which defines the emission timing (5), has largely remained experimentally inaccessible (24). Our work demonstrates that the energy derivative of the quantum phase, which is closely related to the Wigner-Smith time delay (4, 25), can now be accessed by attosecond streaking.

Pushing attosecond timing metrology into the sub–10-as regime has been enabled by waveform-controlled near–single-cycle pulses (duration ~3.3 fs) of near-infrared (NIR, carrier wavelength ~750 nm) light (26). These pulses permit the generation of isolated sub–100-as extreme ultraviolet (XUV) pulses via high-order harmonic generation (12, 14). More importantly for the present study, they increase the XUV photon yield by two orders of magnitude, resulting in an attosecond photon flux (at ~100 eV) in excess of 10^{11} photons/s (14). The resulting more than 10-fold improvement in S/N has advanced the timing accuracy of attosecond streaking to a fraction of the atomic unit of time.

High-order harmonic generation in Ne atoms driven by sub–4-fs NIR pulses yields robust XUV continua in the energy range of 100 to 140 eV, which are stable against substantial changes in the carrier-envelope phase (14). This bandwidth supports isolated pulses below 100 as in duration. Simultaneous temporal characterization of photoemission pathways with distinguishable final ionic states calls for recording streaking spectrograms that are well separated in energy and sets a limit on the XUV bandwidth. To fulfill this condition for the photoelectrons arising from the 2p and 2s subshells of Ne atoms, the spectrum of attosecond pulses is confined with a specially designed lanthanum/molybdenum multilayer XUV mirror and a 150-nm-thick metallic foil. In combination, they act as a bandpass filter centered at 106 eV, with a full width at half maximum of 14 eV, supporting a Fourier-limited XUV pulse duration well below 200 as.

Photoelectrons ejected from Ne atoms by 106-eV attosecond pulses and streaked by the electric field of near–single-cycle NIR pulses were recorded with a time-of-flight spectrometer versus the delay between the XUV and NIR pulses (Fig. 2A). The electron spectrometer

[1]Department für Physik, Ludwig-Maximilians-Universität, Am Coulombwall 1, D-85748 Garching, Germany. [2]Max-Planck-Institut für Quantenoptik, Hans-Kopfermann-Straße 1, D-85748 Garching, Germany. [3]Physik Department, Technische Universität München, James-Franck-Straße, D-85748 Garching, Germany. [4]Theoretical and Physical Chemistry Institute, National Hellenic Research Foundation, 48 Vassileos Constantinou Avenue, Athens 11635, Greece. [5]Institute for Theoretical Physics, Vienna University of Technology, Wiedner Hauptstraße 8-10, 1040 Vienna, Austria. [6]Institute for Theoretical Atomic, Molecular and Optical Physics (ITAMP), Harvard-Smithsonian Center for Astrophysics, Cambridge, MA 02138, USA. [7]Physics and Astronomy Department, King Saud University, Riyadh 11451, Saudi Arabia.

*To whom correspondence should be addressed. E-mail: Martin.Schultze@mpq.mpg.de (M.S.), Vladislav.Yakovlev@physik.uni-muenchen.de (V.S.Y.)

was equipped with an electrostatic lens, enhancing electron counts in the spectral range between 40 and 70 eV. Figure 2B shows the streaking spectrogram reconstructed by the use of an algorithm based on frequency-resolved optical gating (FROG) (27–29). The measured and calculated spectrograms show excellent agreement. Quantitative comparison of streaked spectral lineouts in Fig. 2D demonstrates the high fidelity with which the characteristics of the emitted electron wave packets can be retrieved (30) (Fig. 2C). The evaluated group delay versus frequency reveals that the emission of the electron wave packet from the 2p state lags behind that originating from the 2s state by approximately 20 as. The linear slope of the group delay representing an energy sweep of the emitted electrons potentially provides more insight into photoemission dynamics. We reproducibly observed a difference between the energy sweeps of the 2s and 2p wave packets on the order of several thousand attoseconds squared. Simulations

show, however, that the retrieved energy sweep, in contrast to the average group delay, is sensitive to the electrostatic lens. Hence, the energy sweeps cannot be reliably inferred from the current measurements.

In addition to the FROG approach, we have developed a simplified procedure in order to extract the delay from a large set of measured attosecond streaking spectrograms [for details, see the caption of Fig. 3 and (29)]. Figure 3 summarizes the relative delay extracted from 40 measurements via this method. The result of this analysis agrees within the experimental error with the one obtained with the FROG technique (29). We found a clear correlation between the uncertainty of the evaluated delay and the fractional energy carried by a satellite XUV pulse accompanying the main attosecond pulse. Therefore, we selected a set of delay values evaluated from streaking spectrograms acquired with attosecond XUV pulses exhibiting less than 3% satellite pulse content (red diamonds, Fig. 3).

These data result in a mean relative delay of 21 as between 2p and 2s photoelectrons, with a standard deviation of 5 as. In order to exclude any influence of shakeup states on the evaluated delay, the measurements were repeated using an XUV multilayer mirror with a bandwidth of 4.5 eV centered at ~121 eV (supporting Fourier-limited pulses of ~400 as) in another attosecond beamline. The narrower spectrum of these XUV pulses allowed us to spectrally separate the direct 2s emission line from most of its much weaker high-order shakeup satellites. The results are also plotted in Fig. 3 (green circles) and found, within our error bars, to be in agreement with the ones achieved with sub–200-as pulses.

The measurements summarized in Fig. 3 were performed by applying streaking laser electric fields of different strength, varying by a factor of 6 in amplitude; that is, by a factor of 36 in intensity. In spite of this large dynamic range, the observed delay shows no dependence on the amplitude of the streaking field. The error
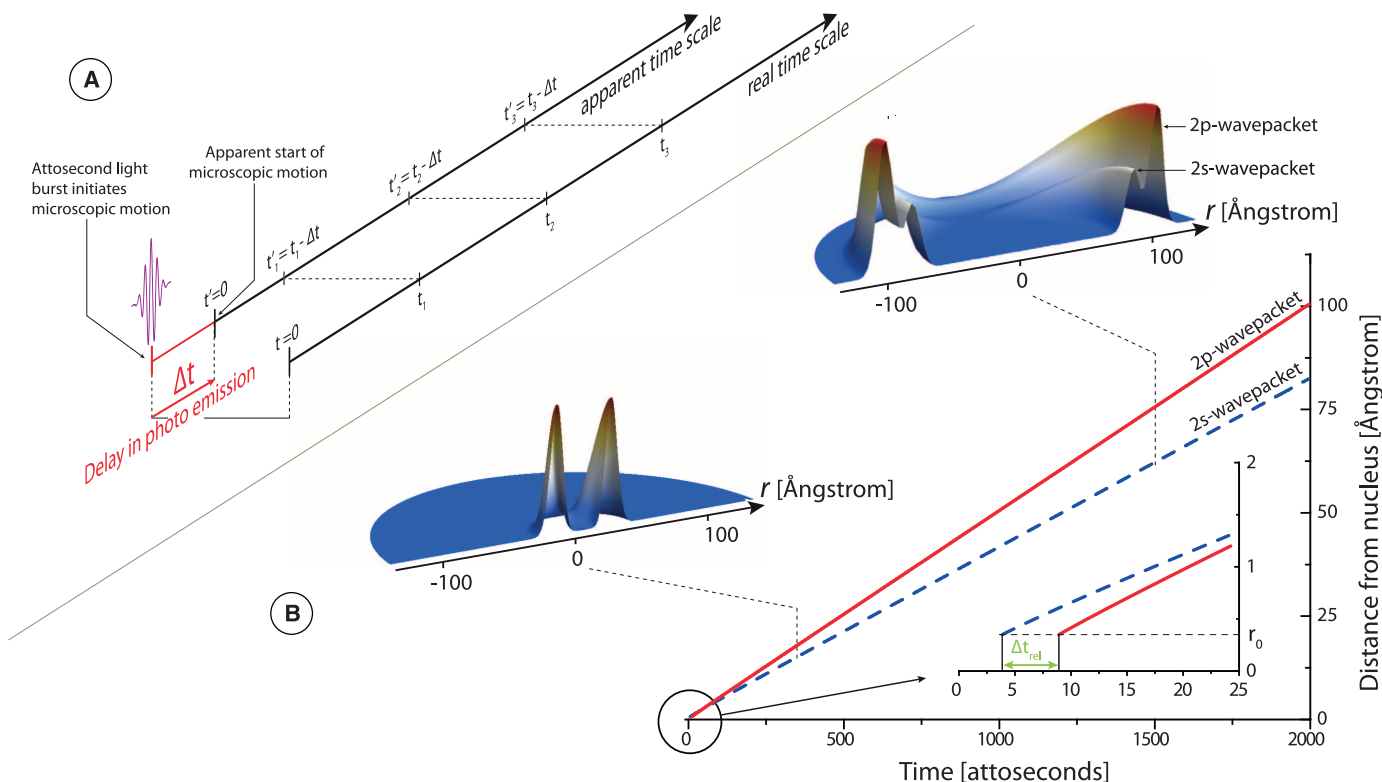
Fig. 1. Attosecond delay in photoemission and its consequences. (**A**) The "real" time scale begins at the maximum of the XUV pulse, whereas the "apparent" time scale in the measurement starts with the release of an electron wave packet and is temporally shifted by a possible delay Δt in photoemission. A delay between the arrival time of the attosecond XUV excitation pulse and the instant of emission would falsify the conclusions reached from measurements with an atomic chronoscope, which is triggered by the emission of an electron wave packet. A microscopic event that occurred at $t = t_{event}$ is indicated by this chronoscope to have apparently happened at $t' = t_{event} - \Delta t$, thereby tainting a comparison between theory and experiment with an unknown systematic error of Δt. (**B**) The surface plots show the spatial distribution of the photoelectron density around the atomic core at $t_1 = 300$ as and $t_2 = 1500$ as after the maximum of the XUV pulse, evaluated by solving

the time-dependent Schrödinger equation with the aid of the state-specific expansion approach. As time progresses, the wave packets released from the 2s and 2p subshells become spatially separated because of their different velocities. Far from the nucleus, where the overlap with ionic orbitals is negligible, their motion can be described semi-classically. Therefore, knowing the average position and velocity of a wave packet that propagates toward the detector, we can illustrate a possible delay in its emission by tracing a classical electron trajectory back to the ion. The red solid and blue dashed lines show the classical trajectories of the 2p and 2s photoelectrons, respectively. The lines terminate at a distance $r_0 \approx 0.3$ Å, which is equal to the radius of the valence shell. At this distance, the trajectories behave as if they started with a relative delay $\Delta t_{rel} = 5$ as, which is in reasonable agreement with the value obtained by a more rigorous theoretical analysis.

bars are reduced at higher intensities, primarily because of the increased spectral shift.

Theoretical discussion. First, we show that the measured delay of ~20 as cannot be explained by a delayed onset of streaking, which was the dominant effect in (*17*). The streaking NIR field may be significantly screened by bound electrons at small distances from the nucleus. After the absorption of an XUV photon, it takes the positive-energy electron a finite time to leave this screened volume, and this time interval may be different for electrons originating from different orbitals. However, for an atom, this difference cannot exceed a few attoseconds. The characteristic scales can be extracted from the classical trajectories shown in Fig. 1B. If we assume that the 2*s* and 2*p* electrons are set in motion at the same moment, their classical

trajectories would acquire a relative delay of 20 as after traveling over 5 Å, whereas significant screening from the streaking field is limited to a distance of less than 1 Å from the nucleus. Furthermore, if screening played a dominant role, the faster 2*p* electrons would be exposed to the streaking field earlier than the slower 2*s* ones, whereas measurements and quantum simulations show that the slower electron is emitted first.

Now we turn our attention to the quantum-mechanical description. First of all, we need a definition for the photoemission delay. Consider a photoelectron wave function $|\psi(t)\rangle$ created by an XUV pulse centered at $t = 0$. The motion of the wave packet after photoionization is conveniently described in a basis of continuum states $|\varepsilon\rangle$, each of which has a well-defined energy ε and describes a wave that propagates in the di-

rection of the detector. In this basis, each probability amplitude has a simple time dependence: $\langle\varepsilon|\psi(t)\rangle = \chi(\varepsilon)e^{-i\frac{\varepsilon}{\hbar}t}$, where the complex-valued function $\chi(\varepsilon)$ fully describes the properties of the wave packet. In this representation, a delay Δt in photoemission, shown as a shift of the electron's trajectory in Fig. 1B, adds $\frac{\varepsilon}{\hbar}\Delta t$ to the phase of $\chi(\varepsilon)$. It is therefore meaningful to define the group delay of the outgoing electron wave packet, in accordance with earlier work (*4*, *5*, *25*), as $\alpha(\varepsilon) = \hbar\frac{d}{d\varepsilon}\arg[\chi(\varepsilon)]$. Analyzing our simulations, we average $\alpha(\varepsilon)$ over the bandwidth of the XUV pulse (*29*) and denote the result as $\overline{\alpha}$.

As the first and most important task, we validate the experimental methodology. Intuitively, one expects that a delay in the formation of a wave packet causes a corresponding temporal shift of the streaking spectrogram. This holds true
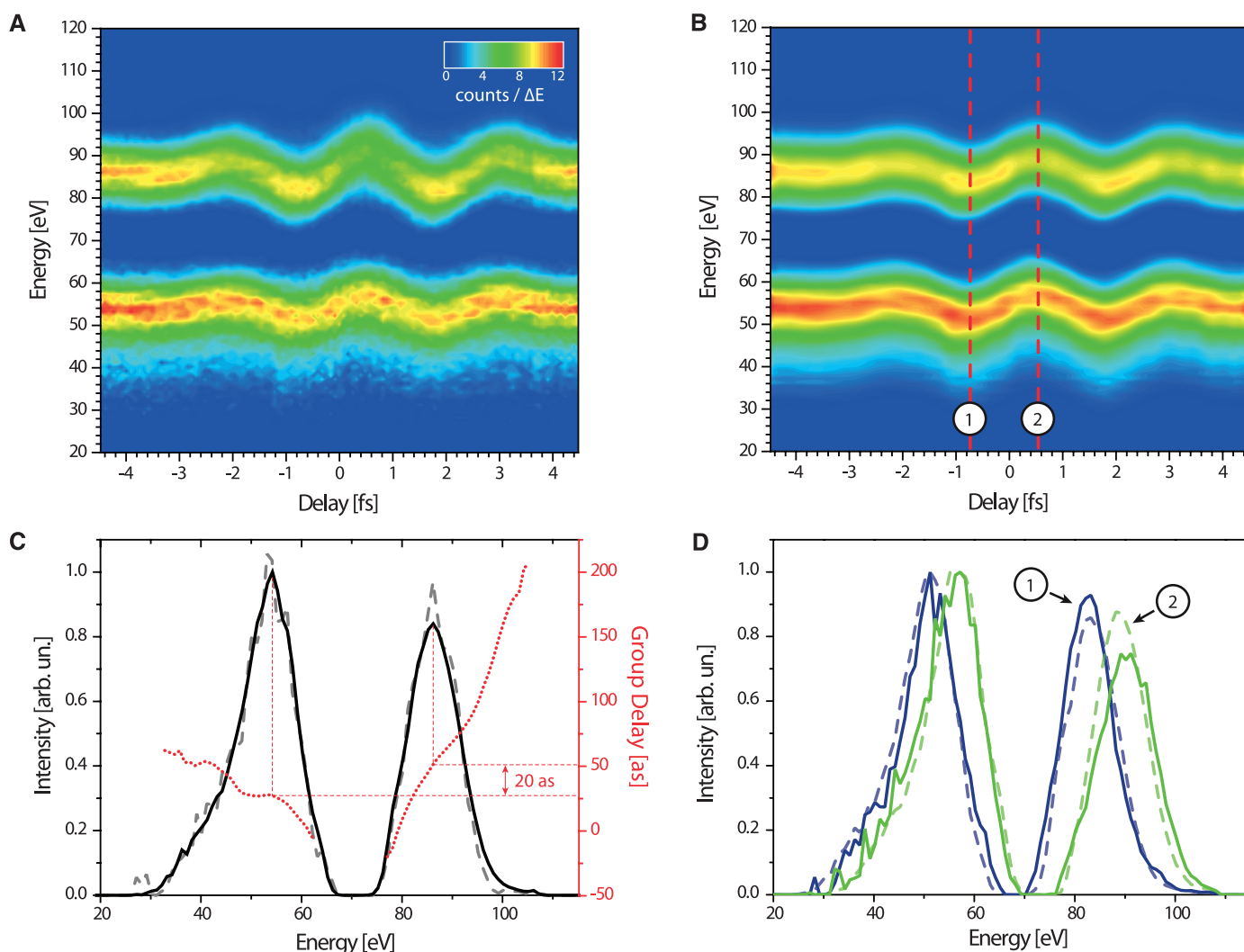

Fig. 2. Attosecond streaking spectrograms (**A** and **B**), evaluated photoelectron wave packets (**C**), and streaked spectra (**D**). The spectrograms in (A) are composed of a series of photoelectron energy spectra recorded by releasing 2*s* and 2*p* electrons from Ne with an attosecond XUV pulse in the presence of a strong NIR few-cycle laser field, as a function of the delay between the XUV and NIR fields. The spectrogram is processed with a FROG algorithm tailored for streaking measurements (*30*). (B) shows the spectrogram reconstructed by this algorithm. The retrieved 2*s* and 2*p* spectra, together with the respective group delays, are plotted in (C) (black solid line and red dotted line, respectively). The reconstructed energy spectra are in excellent agreement with the measured ones (gray dashed line). The average difference between the group delays corresponds to a 20-as retardation of the 2*p* emission with respect to the 2*s* emission. (D) compares reconstructed and measured streaked spectra at two delays, which exhibit the largest positive and negative shifts of the electron energy distribution.

within the Coulomb-Volkov approximation (CVA) (*29*). To quantify the accuracy of the CVA, the single-electron time-dependent Schrödinger equation in three spatial dimensions was numerically solved with an effective potential that modeled Ne (*29*). The analysis of wave packets yielded a spectrally averaged relative group delay of $\overline{a}_{2p} - \overline{a}_{2s} = 4.5$ as. Although the CVA yields the same value of the temporal shift between spectrograms, the numerical solution of the Schrödinger equation results in simulated spectrograms that are shifted with respect to each other by 6.8 as. The origin of this discrepancy lies in the fact that the photoelectron interacts with both the streaking field and the ion, resulting in a quantum motion that is not exactly described by known analytical approaches. Thus, for the current experimental parameters, the small deviations between the electron's exact motion and that modeled via the CVA give rise to a 2-as discrepancy in the relative delay.

Accepting this small discrepancy, many-electron models were applied to investigate the effects of electron correlation. As a first attempt, the multiconfigurational Hartree-Fock method was used to evaluate transition matrix elements from the ground state of Ne to states where the electron wave asymptotically propagated along the direction of the streaking NIR electric field. These matrix elements predict a relative delay of $\overline{a}_{2p} - \overline{a}_{2s} = 4.0$ as. The major drawback of this model is that it does not account for inter-channel coupling (*6*). This deficiency was overcome by modeling the interaction with the XUV pulse using the state-specific expansion approach (*31*, *32*). This model accounts for electron correlations before and after photoionization and predicts a relative group delay of $\overline{a}_{2p} - \overline{a}_{2s} = 6.4$ as. Our modeling successfully predicts that the emission of 2*s* electrons precedes that of 2*p* electrons, but the computed relative delay is ~15 as (3 SD) smaller than the measured value.

So far, the theoretical discussion has focused on the relative delay between two photoemission channels, which can be acquired experimentally. Precise determination of the zero of time for allowing us to track the history of microscopic phenomena accurately (Fig. 1A) calls for precise knowledge of the delay between the XUV pulse and an outgoing electron wave packet (henceforth, absolute delay). This can only be inferred from theory. For multielectron systems, such as Ne, physical description of the discrepancies revealed by this work proved to be a challenge. The sensitive experimental test to which time-dependent many-electron models can now be subjected will benefit their development.
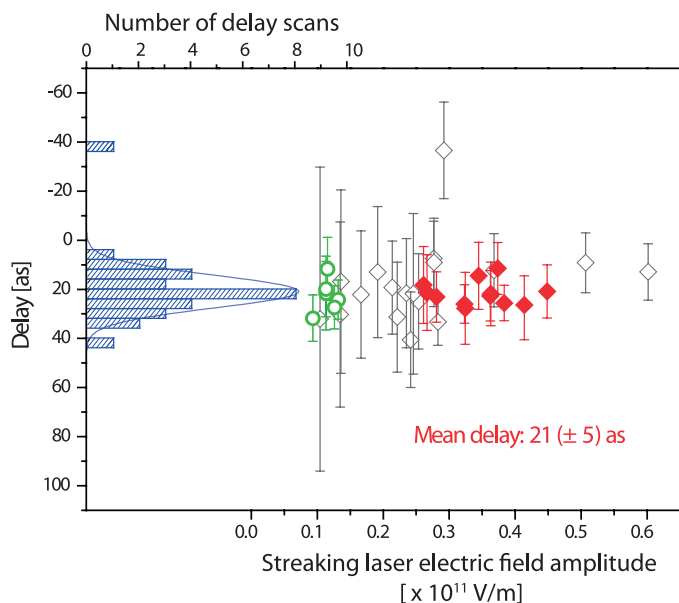
Meanwhile, it is possible to obtain reliable absolute emission times for He, with which truly ab initio simulations (*33*) can be carried out with the help of supercomputers. Such simulations were performed for the He (1*s*²) ground state, and for direct ionization with a 100-eV photon, a 5-as temporal shift of the spectrogram was found. Such modeling will allow precise timing calibration of attosecond measurements, once sufficiently powerful attosecond sources will allow the recording of spectrograms for He with sufficiently good statistics in spite of its small photoionization cross-section.

Conclusions and outlook. Establishing the zero of time in atomic chronoscopy is currently tainted with an error of up to several tens of attoseconds. Because attosecond streaking can measure only relative delays between different photoemission channels, the knowledge of absolute delays relies on the predictions of thoroughly tested time-dependent multielectron models. Presently, only two-electron ab initio simulations provide this degree of reliability, but the low photoionization cross-section of He limits (because of low *S/N*) the timing accuracy. For more complex systems, phase-sensitive measurements of the photoelectron wave packets via attosecond streaking will put many-electron models of atomic photoionization to comprehensive, highly sensitive tests, which is a prerequisite for gradually improving them and gaining trust in their predictions. These developments will improve our understanding of subatomic electron correlations and will make the absolute timing precision of atomic chronoscopy approach the 1-as frontier.

Fig. 3. The relative delay between photoemission from the 2*p* and 2*s* subshells of Ne atoms, induced by sub–200-as, near–100-eV XUV pulses. The depicted delays are extracted from measured attosecond streaking spectrograms by fitting a spectrogram, within the strong-field approximation, with parameterized NIR and XUV fields. Our optimization procedure matches the first derivatives along the time delay dimension of the measured and reconstructed spectrograms, thereby eliminating the influence of unstreaked background electrons [for details on the fitting algorithm, see (*29*)]. From the analysis of a set of spectrograms, the measured delays and associated retrieval uncertainties are plotted against the amplitude of the vector potential applied in the attosecond streak camera. Spectrograms measured in the presence of a satellite attosecond pulse were found to exhibit a less accurate retrieval of the delay value. When a subset of data (red diamonds) that represents scans with less than 3% satellite pulse content was evaluated, a mean delay value of 21 as with a standard deviation of ~5 as was found. The green circles represent the result of analyzing spectrograms recorded with an XUV pulse with narrower bandwidth in order to exclude the potential influence of shakeup states contributing to the electron kinetic energy spectrum.

References and Notes
1. H. Hertz, *Annalen Physik Chem.* **267**, 983 (1887).
2. W. Hallwachs, *Annalen Physik Chem.* **269**, 301 (1888).
3. A. Einstein, *Annalen Physik* **17**, 132 (1905).
4. E. P. Wigner, *Phys. Rev.* **98**, 145 (1955).
5. C. A. A. de Carvalho, H. M. Nussenzveig, *Phys. Rep.* **364**, 83 (2002).
6. A. F. Starace, in *Handbuch der Physik*, W. Mehlhorn, Ed. (Springer, Berlin, 1982), vol. 31.
7. S. T. Manson, *Radiat. Phys. Chem.* **75**, 2119 (2006).
8. M. Y. Ivanov, J. P. Marangos, *J. Mod. Opt.* **54**, 899 (2007).
9. A. Baltuška *et al.*, *Nature* **421**, 611 (2003).
10. R. Kienberger *et al.*, *Nature* **427**, 817 (2004).
11. M. Nisoli, G. Sansone, *Prog. Quantum Electron.* **33**, 17 (2009).
12. G. Sansone *et al.*, *Science* **314**, 443 (2006).
13. M. Schultze *et al.*, *N. J. Phys.* **9**, 243 (2007).
14. E. Goulielmakis *et al.*, *Science* **320**, 1614 (2008).
15. M. Hentschel *et al.*, *Nature* **414**, 509 (2001).
16. A. Borisov, D. Sánchez-Portal, R. Díez Muiño, P. M. Echenique, *Chem. Phys. Lett.* **387**, 95 (2004).
17. A. L. Cavalieri *et al.*, *Nature* **449**, 1029 (2007).
18. A. K. Kazansky, P. M. Echenique, *Phys. Rev. Lett.* **102**, 177401 (2009).
19. C. Lemell, B. Solleder, K. Tőkési, J. Burgdörfer, *Phys. Rev. A* **79**, 062901 (2009).
20. J. C. Baggesen, L. B. Madsen, *Phys. Rev. Lett.* **104**, 043602; and erratum, 209903 (2010).
21. U. Becker, D. A. Shirley, in *VUV and Soft X-Ray Photoionization*, U. Becker, D. A. Shirley, Eds. (Plenum, New York, 1997), chap. 5.
22. A. Rudenko *et al.*, *Phys. Rev. Lett.* **101**, 073003 (2008).
23. J. Mauritsson *et al.*, *Phys. Rev. Lett.* **100**, 073003 (2008).

24. The relative phases of interfering partial waves are accessible to measurement because they determine angular photoelectron distributions; still, this information is not sufficient to retrieve either the energy dependence of a phase in a particular photoionization channel or the relative phase between channels that do not interfere.
25. F. T. Smith, *Phys. Rev.* **118**, 349 (1960).
26. A. L. Cavalieri *et al.*, *N. J. Phys.* **9**, 242 (2007).
27. Y. Mairesse, F. Quéré, *Phys. Rev. A* **71**, 011401 (2005).
28. J. Gagnon, E. Goulielmakis, V. S. Yakovlev, *Appl. Phys. B* **92**, 25 (2008).
29. Information on technology and methods is available as supporting material on *Science* Online.
30. J. Gagnon, V. S. Yakovlev, *Opt. Express* **17**, 17678 (2009).
31. C. A. Nicolaides, Th. Mercouris, Y. Komninos, *J. Phys. At. Mol. Opt. Phys.* **35**, L271 (2002).
32. Th. Mercouris, Y. Komninos, C. A. Nicolaides, *Phys. Rev. A* **76**, 033417 (2007).
33. J. S. Parker, B. J. S. Doherty, K. J. Meharg, K. T. Taylor, *J. Phys. At. Mol. Opt. Phys.* **36**, L393 (2003).
34. Supported by the Max Planck Society and the Deutsche Forschungsgemeinschaft Cluster of Excellence: Munich Centre for Advanced Photonics (www.munich-photonics.de) and the King Saud University–Max-Planck-Institut für Quantenoptik collaboration. Supported in part by NSF through TeraGrid resources provided by the National Institute for Computational Sciences and Texas Advanced Computing Center under grant TG-PHY090031. R.P., S.N., and J.B. acknowledge support from the Austrian Science Fund (FWF) under grant FWF-SFB016. J.F. acknowledges support by NSF through a grant to ITAMP. E.G. acknowledges a Marie-Curie Reintegration grant (MERG-CT-2007-208643). R.K. acknowledges support from the Sofia Kovalevskaja award of the Alexander von Humboldt Foundation and an ERC starting grant. We thank A. Maquet and R. Taïeb for fruitful discussions.

Reconstituting Organ-Level Lung Functions on a Chip

Dongeun Huh,[1,2] Benjamin D. Matthews,[2,3] Akiko Mammoto,[2] Martín Montoya-Zavala,[1,2] Hong Yuan Hsin,[2] Donald E. Ingber[1,2,4]*

Here, we describe a biomimetic microsystem that reconstitutes the critical functional alveolar-capillary interface of the human lung. This bioinspired microdevice reproduces complex integrated organ-level responses to bacteria and inflammatory cytokines introduced into the alveolar space. In nanotoxicology studies, this lung mimic revealed that cyclic mechanical strain accentuates toxic and inflammatory responses of the lung to silica nanoparticles. Mechanical strain also enhances epithelial and endothelial uptake of nanoparticulates and stimulates their transport into the underlying microvascular channel. Similar effects of physiological breathing on nanoparticle absorption are observed in whole mouse lung. Mechanically active "organ-on-a-chip" microdevices that reconstitute tissue-tissue interfaces critical to organ function may therefore expand the capabilities of cell culture models and provide low-cost alternatives to animal and clinical studies for drug screening and toxicology applications.

One of the causes of the high cost of pharmaceuticals and the major obstacles to rapidly identifying new environmental toxins is the lack of experimental model systems that can replace costly and time-consuming animal studies. Although considerable advances have been made in the development of cell culture models as surrogates of tissues and organs for these types of studies (*1*), cultured cells commonly fail to maintain differentiation and expression of tissue-specific functions. Improved tissue organization can be promoted by growing cells in three-dimensional extracellular matrix (ECM) gels (*2*); however, these methods still fail to reconstitute structural and mechanical features of whole living organs that are central to their function. In particular, existing model systems do not recreate the active tissue-tissue interface between the microvascular endothelium and neighboring parenchymal tissues where critical transport of fluids, nutrients, immune cells, and other regulatory factors occur, nor do they permit application of dynamic mechanical forces (e.g., breathing movements in lung, shear in blood vessels, peristalsis in gut, tension in skin, and the like) that are critical for the development and function of living organs (*3*).

Microscale engineering technologies first developed to create microchips, such as microfabrication and microfluidics, enable unprecedented capabilities to control the cellular microenvironment with high spatiotemporal precision and to present cells with mechanical and biochemical signals in a more physiologically relevant context (*4–7*). This approach has made it possible to microfabricate models of blood vessels (*8, 9*), muscles (*10*), bones (*11*), airways (*12*), liver (*13–16*), brain (*17, 18*), gut (*19*), and kidney (*20, 21*). However, it has not yet been possible to engineer integrated microsystems that replicate the complex physiological functionality of living organs by incorporating multiple tissues, including active vascular conduits, and placing them in a dynamic and mechanically relevant organ-specific microenvironment.

To provide the proof of principle for a biomimetic microsystems approach, we developed a multifunctional microdevice that reproduces key structural, functional, and mechanical properties of the human alveolar-capillary interface, which is the fundamental functional unit of the living lung. This was accomplished by microfabricating a microfluidic system containing two closely apposed microchannels separated by a thin (10 μm), porous, flexible membrane made of poly(dimethylsiloxane) (PDMS). The intervening membrane was coated with ECM (fibronectin or collagen), and human alveolar epithelial cells and human pulmonary microvascular endothelial cells were cultured on opposite sides of the membrane (Fig. 1A). Once the cells were grown to confluence, air was introduced into the epithelial compartment to create an air-liquid interface and more precisely mimic the lining of the alveolar air space. The compartmentalized channel configuration of the microdevice makes it possible to manipulate fluid flow, as well as delivery of cells and nutrients, to the epithelium and endothelium independently.

During normal inspiration, intrapleural pressure decreases, causing the alveoli to expand; this pulls air into the lungs, resulting in stretching of the alveolar epithelium and the closely apposed endothelium in adjacent capillaries (Fig. 1B). We mimicked this subatmospheric, pressure-driven stretching by incorporating two larger, lateral microchambers into the device design. When vacuum is applied to these chambers, it produces elastic deformation of the thin wall that separates the cell-containing microchannels from the side chambers; this causes stretching of the attached PDMS membrane and the adherent tissue layers (Fig. 1A, right versus left). When the vacuum is released, elastic recoil of PDMS causes the membrane and adherent cells to relax to their original size. This design replicates dynamic mechanical distortion of the alveolar-capillary interface caused by breathing movements.

These hollow microchannels were fabricated by soft lithography in conjunction with a new method that uses chemical etching of PDMS (*22*) to form the vacuum chambers. Fabrication begins with alignment and permanent bonding of a 10-μm-thick porous PDMS membrane (containing 10-μm-wide pentagonal pores) and two PDMS layers containing recessed microchannels (Fig. 1C). A PDMS etching solution composed of tetrabutyl-

[1]Wyss Institute for Biologically Inspired Engineering at Harvard University, Boston, MA 02115, USA. [2]Vascular Biology Program, Departments of Pathology and Surgery, Children's Hospital Boston, and Harvard Medical School, Boston, MA 02115, USA. [3]Department of Medicine, Children's Hospital Boston, Boston, MA 02115, USA. [4]School of Engineering and Applied Sciences, Harvard University, Cambridge, MA 02138, USA.

*To whom correspondence should be addressed. E-mail: don.ingber@wyss.harvard.edu